RSC Advances

PAPER

View Article Online
View Journal | View Issue



Cite this: *RSC Adv.*, 2025, **15**, 2066

# Structural and luminescent properties of a $Cr^{3+}/Sm^{3+}$ doped $GdAlO_3$ orthorhombic perovskite for solid-state lighting applications

I. Elhamdi, *[ae] H. Souissi, [a] S. Kammoun, [a] E. Dhahri, [a] J. Pina,[b] B. F. O. Costa, [c] A. L. B. Brito,[b] R. Fausto [bd] and E. López-Lago [e]

Received 30th December 2024
Accepted 11th January 2025

DOI: 10.1039/d4ra09098e

rsc.li/rsc-advances

The $Cr^{3+}$ and $Sm^{3+}$ doped $GdAlO_3$ perovskite with formula $Gd_{0.995}Sm_{0.005}Al_{0.995}Cr_{0.005}O_3$, was synthesized *via* a solid-state reaction method, and its structure, morphology, and photoluminescence properties were thoroughly investigated. The compound crystallizes in the orthorhombic *Pbnm* space group, with $Cr^{3+}$ transition-metal ions substituting $Al^{3+}$ in the octahedral symmetry site, and $Sm^{3+}$ lanthanide (rare-earth) ions occupying the tetrahedral site. The material's morphology and chemical composition homogeneity were evaluated through Scanning Electron Microscopy (SEM) and Energy Dispersive X-ray analysis. Photoluminescence excitation (PLE) and emission spectra (PL) were used to shed light on the electronic structure of the $Cr^{3+}$ cations, through crystal field analysis in the $O_h$ symmetry site. Theoretical studies enabled the precise assignment of the $Cr^{3+}$ 3d–3d transitions. The intra-configurational 4f–4f transitions of $Sm^{3+}$ resulted in a variety of excitation bands appearing in the high-wavelength range of the PLE spectrum. The photoluminescence studies supported the occurrence of energy transfer in the doped $GdAlO_3$ perovskite between $Gd^{3+}$, $Sm^{3+}$ and $Cr^{3+}$ ions. The obtained results suggest the high potential of the synthesized material for solid state lighting applications.



## 1. Introduction

The investigation of rare-earth-doped luminescent materials has unlocked new avenues of innovation, driving advancements across various high-tech industries.[1] Among these, white light-emitting devices (LEDs) stand out due to their exceptional luminescent properties. In the context of global energy challenges and the growing threat of climate change, the need for innovative and efficient phosphors tailored for solid-state lighting (SSL) is critical.[2,3] The demand for novel phosphors used in SSL displays and lamps continues to rise, driven by their prolonged lifespan, high luminescence efficiency, and contribution to sustainable environmental practices.[4–8]

Aluminate-based host matrices have garnered significant attention as ideal candidates for phosphor development due to their superior crystallinity, excellent luminous characteristics, straightforward synthesis, favorable color parameters, and exceptional chemical and thermal stability. Their high heat resistance further enhances their suitability for doping with various ions, enabling the creation of materials optimized for diverse applications.[9,10] Consequently, aluminate-based materials have been extensively investigated and have found applications in energy harvesting for flat-panel displays,[11] SSL,[12] scintillators,[13] optical lasers,[14] light-emitting diodes,[15] photonic storage devices, and remote sensing technologies.[16]

Among these materials, gadolinium aluminate ($GdAlO_3$), featuring an orthorhombic perovskite crystal structure (*Pnma* space group), is a particularly notable example. $GdAlO_3$ is uniquely suited for multifunctional applications due to its robust thermal and chemical stability, compatibility with rare-earth dopants, and excellent energy transfer characteristics. These properties make it an attractive host matrix for developing phosphors with tailored optical and magnetic functionalities. While gadolinium can be expensive, the strategic use of $GdAlO_3$ in doped compositions mitigates costs,[17] and its performance advantages justify its use in niche applications such as magneto-optoelectronics and hybrid devices requiring simultaneous photoluminescent and magnetic properties.[18–20] Furthermore, $GdAlO_3$ based materials show promise for energy storage and conversion technologies, adding to their appeal as next-generation phosphor materials.

$Cr^{3+}$ ions were selected as primary activators due to their well-established photoluminescent properties, including intense and tunable red emissions. To further enhance the

[a]*Applied Physics Laboratory, Faculty of Sciences, Sfax University, BP 1171, 3000, Sfax, Tunisia. E-mail: imen85356@gmail.com*

[b]*University of Coimbra, CQC-IMS, Chemistry Department, 3004-535 Coimbra, Portugal*

[c]*University of Coimbra, CFisUC, Physics Department, 3004-516 Coimbra, Portugal*

[d]*Faculty of Sciences and Letters, Department of Physics, Istanbul Kultur University, Ataköy Campus, Bakirköy 34156, Istanbul, Turkey*

[e]*Departamento de Física Aplicada, Facultade de Óptica e Optometríae Instituto de Materiais (iMATUS) Campus Vida, Universidade de Santiago de Compostela (USC), 15782 Galicia, Spain*

material's spectral characteristics, $Sm^{3+}$ was introduced as a codopant. $Sm^{3+}$ was chosen for its ability to enhance red luminescence and its potential to act as an energy transfer mediator, facilitating a synergistic effect with $Cr^{3+}$. This combination is particularly relevant for applications requiring optimized spectral output, such as full-spectrum lighting or display technologies. Moreover, the dopant combination leverages the perovskite structure of $GdAlO_3$ to enable efficient energy transfer and tailored luminescent properties.

In this investigation, we synthesized and characterized the structural and luminescence properties of a $Cr^{3+}$ doped orthorhombic $GdAlO_3$ perovskite phosphor, codoped with $Sm^{3+}$ to achieve the composition $Gd_{0.995}Sm_{0.005}Al_{0.995}Cr_{0.005}O_3$. This study aims to elucidate the fundamental mechanisms governing the optical properties of $GdAlO_3$ doped with $Cr^{3+}$ and $Sm^{3+}$, thereby fostering further exploration into the potential of complex oxides doped with transition and rare-earth elements for advanced technological applications. The findings presented here demonstrate the promise of this novel material for applications in solid-state lighting.

## 2. Materials and methods

In this study, $GdAlO_3$ perovskite was synthesized *via* solid-state method. High-purity gadolinium oxide ($Gd_2O_3$) and aluminum oxide ($Al_2O_3$) powders were weighted in stoichiometric ratio to form the base material. To introduce chromium and samarium doping, appropriate amounts of samarium oxide ($Sm_2O_3$) and chromium oxide ($Cr_2O_3$) were added, ensuring the desired doping level of $Gd_{0.995}Sm_{0.005}Al_{0.995}Cr_{0.005}O_3$. The solid-state method was chosen for its robustness and ability to exert precise control over reaction conditions. Following pre-annealing at 700 °C for 24 hours to remove volatile inorganic materials, the mixture was ground using an agate mortar and pestle to ensure intimate mixing of the reactants. The resulting mixture was then sintered at 1200 °C for 24 hours, promoting atomic and ionic diffusion essential for the formation of the desired doped $GdAlO_3$ compound. The high temperature during sintering facilitated the incorporation of $Cr^{3+}$ and $Sm^{3+}$ ions into the crystal lattice, ensuring the development of the desired orthorhombic crystal structure. Finally, the sintered material was compacted into pellets with a diameter of 8 mm, which were used in the subsequent characterization and analyses experiments.

Characterization of the newly synthesized compound was undertaken using different techniques. The material was first analyzed by powder X-ray diffraction (X-ray Siemens D5000, with $\lambda = 1.5406$ Å $CuK_\alpha$ radiation). Data was collected within the 20–100° $2\theta$ range, with a step size of 0.02°. Subsequently, photoluminescence emission (PL) and excitation (PLE) measurements were collected in a Horiba-Jobin-Yvon Fluorolog 322, operating in time-resolved mode (using a pulsed lamp) with a 0.05 ms delay after-flash. The morphology of the material and its chemical homogeneity were investigated by scanning electron microscopy (SEM), using a TESCAN VEGA3 SBH instrument equipped with an X-ray energy dispersive microscopy (EDS) detector. Image analysis was carried out using the ImageJ software,[21] and structure analysis was undertaken using the Visualization Electronic and Structural Analysis (VESTA) software.[22–24]

Raman spectra were collected (with 4 $cm^{-1}$ spectral resolution) in a LabRAM HR Evolution Raman microscope (Horiba Scientific) with a 600 g $mm^{-1}$ grating. The excitation was provided by a He–Ne laser ($\lambda = 633$ nm), which was focused on the sample to a ~1 mm spot using a 100× objective. The applied laser power of ~0.2 mW at the sample resulted in no detectable heating or degradation. The collection time was 10 s with 100 accumulations being averaged to generate the final spectra.

The chromaticity coordinates ($x$, $y$) of the synthesized $Gd_{0.995}Sm_{0.005}Al_{0.995}Cr_{0.005}O_3$ phosphor were determined using the CIE 1931 color space from its emission spectrum under 377 nm excitation. The correlated color temperature (CCT) and color purity (CP) values were calculated based on established methods.[25,26] The resulting parameters are presented in Table 1, demonstrating the material's potential for applications in warm white light-emitting diodes (LEDs).

Fig. 1 shows the CIE 1931 chromaticity diagram for the $Gd_{0.995}Sm_{0.005}Al_{0.995}Cr_{0.005}O_3$ phosphor, generated from the emission spectrum under 377 nm excitation, where the coordinates are positioned in the reddish-orange region.

Table 1 CIE parameters for the red luminescence color of the synthesized $Cr^{3+}/Sm^{3+}$ doped $GdAlO_3$ phosphor

| $x$ | $y$ | CCT (K) | CP (%) |
|---|---|---|---|
| 0.62157 | 0.37383 | 1892.46 | 87.08 |

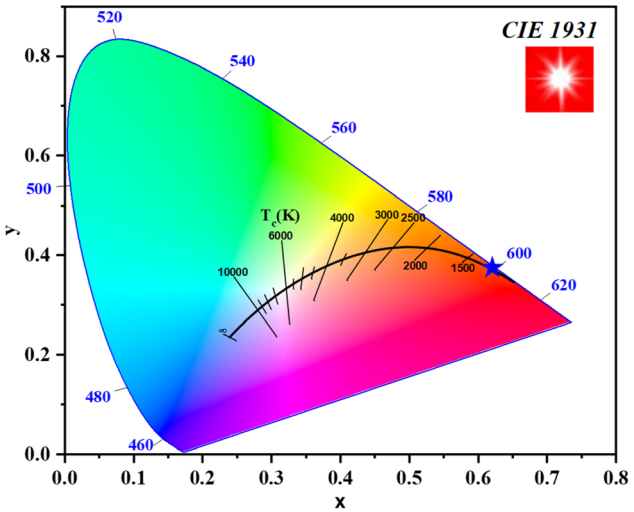


Fig. 1 The CIE graph for the studied $Cr^{3+}/Sm^{3+}$ doped $GdAlO_3$ phosphor.

## 3. Results and discussion

### 3.1 Powder X-ray diffraction analyses

Powder X-ray diffraction (PXRD) is a powerful technique for elucidating crystal phases, lattice parameters, and overall

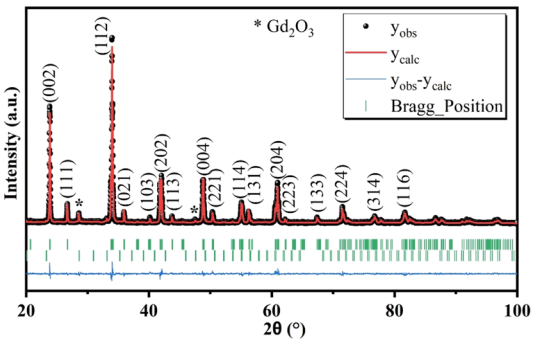


Fig. 2 Results of the performed Rietveld refinement for $Gd_{0.995}Sm_{0.005}Al_{0.995}Cr_{0.005}O_3$.

structural characteristics of solid materials. To determine the phases present in the synthesized material, its PXRD diffraction pattern (Fig. 2) was obtained and compared with ICDD (International Center for Diffraction Data) database. The observed peaks could be successfully indexed to a primitive orthorhombic crystal lattice, within the *Pbnm* space group. The identification process used standard JCPDS data files [$GdAlO_3$ 46-0395; $Gd_2O_3$ 88-2165]. Rietveld refinement revealed the presence of two phases, the predominant one corresponding to the perovskite compound and the minor to $Gd_2O_3$. The presence of the $Gd_2O_3$ as impurity in the sample is consistent with previous studies,[27] where this impurity was also observed. Table 2 presents the refined crystallographic parameters, with the agreement between calculated and observed profiles being satisfactory, as indicated by a $\chi^2$ value of 1.7. The fit quality between the observed and calculated diffraction patterns is reflected by $R_p = 17.6$, $R_{wp} = 14.2$, and $R_e = 10.9$. While, $R_p$ (profile *R*-factor) is a measure of the agreement between the observed and calculated diffraction profiles, $R_{wp}$ (weighted profile *R*-factor) is similar to $R_p$ but takes into account the statistical weights of the observed intensities and $R_e$ (expected *R*-factor) represents the ideal *R*-factor that would be obtained if the model perfectly fits the data, considering only statistical uncertainties. Fig. 3 depicts the structures of the $GdAlO_3$ perovskite, where $Al^{3+}$ and $Gd^{3+}$ cations are bonded to six and eight oxygen atoms, respectively. $Al^{3+}$ ions occupy an octahedral ($O_h$) coordination site corresponding to corner-sharing $AlO_6$ octahedra with tilt angles of 24°, while $Gd^{3+}$ stay in a coordination site whose symmetry is $C_s$. The compound presents four shorter and two longer Al–O bond lengths, along with two inequivalent $O^{2-}$ sites. In the first site, $O^{2-}$ is bonded in a 5-coordination geometry to three equivalent $Gd^{3+}$ and two equivalent $Al^{3+}$ cations; in the second, $O^{2-}$ is bonded in a 4-

Table 2 Cell parameters and volume resulting from the Rietveld refinement for the synthesized compound, and statistical indicators

| | | | |
|---|---|---|---|
| Formula | $Gd_{0.995}Sm_{0.005}Al_{0.995}Cr_{0.005}O_3$ | $R_p$ | 17.6 |
| Space group | *Pbnm* | $R_{wp}$ | 14.2 |
| *a* (Å) | $5.251_7$ | $R_e$ | 10.9 |
| *b* (Å) | $5.299_8$ | $\chi^2$ | 1.7 |
| *c* (Å) | $7.445_8$ | $Gd_2O_3$ (%) | $3.050_1$ |
| *V* (Å$^3$) | $207.240_1$ | SEM (nm) | 177 |

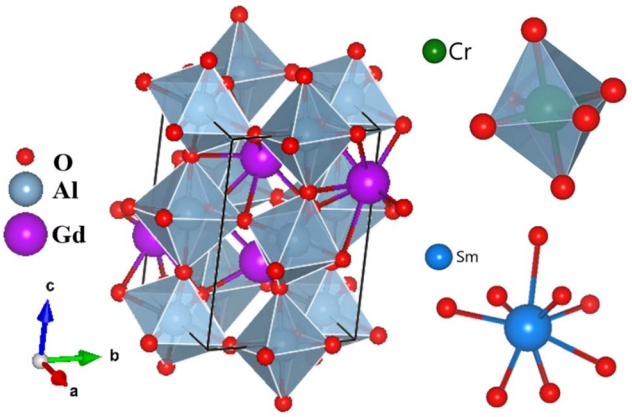


Fig. 3 Illustration (Vesta software images) of the structure of the $GdAlO_3$ perovskite, and of the 8-coordinated $SmO_8$ and 6-coordinated (octahedral) $CrO_6$ units.

coordination geometry to two equivalent $Gd^{3+}$ and two equivalent $Al^{3+}$ cations. Upon doping, $Cr^{3+}$ and $Sm^{3+}$ cations are hypothesized to replace $Al^{3+}$ and $Gd^{3+}$, respectively, due to the close match in their ionic radii. $Cr^{3+}$ (0.615 Å in octahedral coordination) is similar in size to $Al^{3+}$ (0.535 Å), making it a suitable substitute at the $Al^{3+}$ site. Similarly, the ionic radius of $Sm^{3+}$ (1.079 Å in nine-fold coordination) closely matches that of $Gd^{3+}$ (1.053 Å), facilitating substitution at the $Gd^{3+}$ site.

### 3.2 EDS and particles morphology studies

Scanning electron microscopy (SEM) was employed to investigate the morphology of particles of the synthesized compound. Fig. 4 shows the presence of agglomerated and irregularly

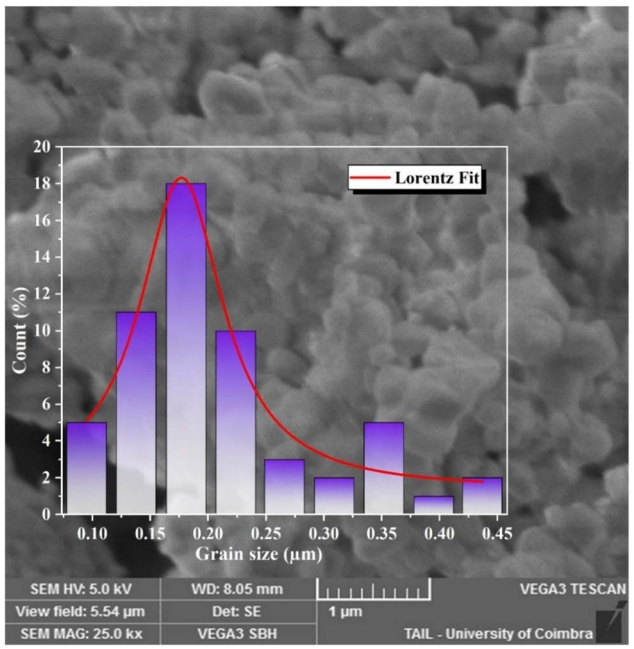


Fig. 4 SEM image and particle size distribution histogram of the synthesized compound, and results of the Lorentz fit to the distribution data.

shaped grains, resulting from the substantial surface area of the particles and their interaction *via* weak van der Waals forces. The average particle size distribution, determined by Lorentz fitting using the ImageJ software, shows a peak centered at 177 nm.

To confirm the chemical composition of the sample, its EDS spectrum was collected (Fig. 5). The spectrum exhibits characteristic peaks of all expected elements (Gd, Cr, Al, Sm, O) confirming the presence of these elements in the sample. The low-energy peaks correspond to lighter elements like Al and O, while the intermediate-energy peaks are attributed to Cr, Sm, and Gd, with distinct signals from their L and K edges. High-energy peaks, primarily from the K edges of Gd, also show some overlap from Sm, consistent with their atomic characteristics. All peaks are clearly labeled in the spectrum for clarity.

The elemental distribution maps, presented in the smaller images on the right of Fig. 5, provide a visual representation of the spatial distribution of the elements in the sample. While the main inset (colorful grain map) shows some inhomogeneity in the intensity of elemental signals, this variation is likely due to factors such as sample morphology, local concentration differences, or surface roughness, which can affect signal intensities. Despite these minor variations, the maps demonstrate significant co-localization of the elements, indicating a uniform distribution across the sample. This is further supported by the composite overlay of the elemental maps, where no regions are completely absent of any detected elements, confirming the overall homogeneity of the elemental distribution.

Table 3 provides the results of the quantitative analysis of the elements present in the sample, which show good agreement with the theoretical values for the expected composition. The observed differences between the nominal composition and EDS results, particularly for Cr and Sm, are attributed to the limitations of EDS in quantifying trace elements and matrix effects. Despite these minor discrepancies, the elemental maps confirm a homogeneous distribution of elements across the sample.

Table 3 Elemental composition obtained from the EDS data of the studied sample and theoretical values for $Gd_{0.995}Sm_{0.005}Al_{0.995}Cr_{0.005}O_3$

| Element | Series | Experimental (weight%) | Error (%) | Theoretical (weight%) | Experimental (atomic%) |
|---|---|---|---|---|---|
| Al | K | 16.19 | 1.61 | 14.57 | 17.56 |
| Cr | K | 0.30 | 0.09 | 0.14 | 0.23 |
| Sm | L | 2.92 | 0.18 | 0.41 | 1.13 |
| Gd | L | 80.59 | 3.92 | 84.88 | 81.08 |
| Total | | 100.00 | | 100.00 | 100.00 |

### 3.3 Raman spectroscopy analyses

The symmetry analyses of *Pbnm* space group symmetry perovskites of general formula $ABO_3$ has been detailed by Chopelas, who has performed a systematic study of the Raman spectra of 30 different aluminate orthorhombic perovskites with emphasis on $YAlO_3$ and $GdAlO_3$.[28] In the Brillouin zone center, the 24 Raman active optical modes span the symmetry species $7A_g + 7B_{1g} + 5B_{2g} + 5B_{3g}$. Chopelas has observed and assigned twenty of these modes for $GdAlO_3$ using single crystal polarized Raman spectroscopy with excitation at 488.0 or 457.9 nm ($Ar^+$ laser).[28]

The Raman spectra of $GdAlO_3$ and of the synthesized $Gd_{0.995}Sm_{0.005}Al_{0.995}Cr_{0.005}O_3$ compound obtained in the present study using 633 nm excitation are shown in Fig. 6, together with the difference spectrum obtained by subtracting

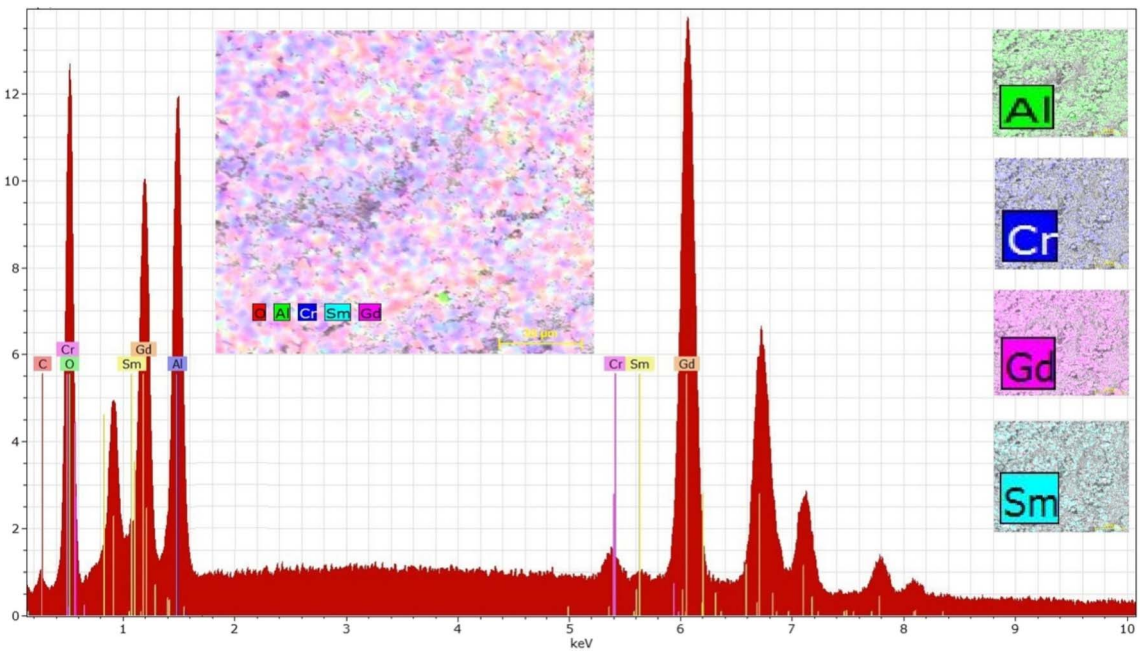


Fig. 5 EDS spectrum of $Gd_{0.995}Sm_{0.005}Al_{0.995}Cr_{0.005}O_3$ and elements distribution maps.

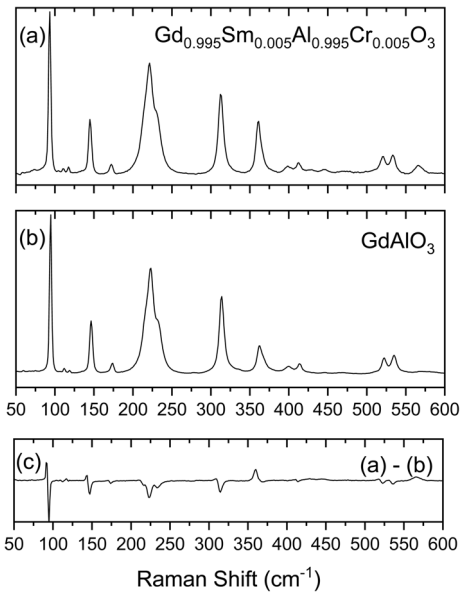


Fig. 6 Raman spectra of the prepared compound (a) compared to that of undoped $GdAlO_3$ (b). Plot (c) is the difference spectrum obtained by subtracting the spectrum of the undoped $GdAlO_3$ perovskite from that of the prepared compound.

the spectrum of the undoped $GdAlO_3$ perovskite from that of the newly prepared compound. The difference spectrum allows to better notice the spectral changes due to the presence of the dopant atoms, which for most of the bands correspond to small shifts to lower frequency. These changes could be anticipated considering the much larger mass of chromium compared to aluminum (51.996 *vs.* 26.9815). On the other hand, the mass difference between gadolinium and samarium is small (157.2 *vs.* 150.4) so that the effects of the substitution of $Gd^{3+}$ ions by $Sm^{3+}$ at the level of substitution in the studied compound could be expected to lead to experimentally non-detectable perturbations in the frequencies of the modes where the movements of these atoms play a major role.

The collected spectrum of the undoped $GdAlO_3$ compound follows closely those reported before.[28,29] Assignments are given in Table 4, which includes also the data for the studied $Sm^{3+}$/$Cr^{3+}$ doped compound. Compared to the previous investigations,[28,29] the present results have allowed to propose assignments for the 4 modes not yet firmly assigned before: the assignment of the $A_g$ mode 6 proposed by Gouadec *et al.*[29] was confirmed to the band now located at 445.0 $cm^{-1}$ (440 $cm^{-1}$ as reported before[29]), and the $B_{1g}$ modes 4 and 6 are assigned to bands observed at 280.0 and 570.0 $cm^{-1}$, respectively, at frequencies in the ranges observed for other orthorhombic *Pbnm* aluminium oxide perovskites;[29] the $B_{2g}$ mode 1 that had been previously ascribed to the band at 146 $cm^{-1}$, is now reassigned to the band observed at 119.0 $cm^{-1}$, while the band at 146 $cm^{-1}$ is reassigned to the $B_{2g}$ mode 2 (this band is also assigned to the $A_g$ mode 2, following the assignments proposed

Table 4 Assignment of the Raman spectra of $GdAlO_3$ and of $Gd_{0.995}Sm_{0.005}Al_{0.995}Cr_{0.005}O_3$

| | | $GdAlO_3$ | | | $Gd_{0.995}Sm_{0.005}Al_{0.995}Cr_{0.005}O_3$ |
|---|---|---|---|---|---|
| Symmetry | Mode | This study | 28 | 29 | This study |
| $A_g$ | 1 | 94.5 | 95 | 93.5 | 93.0 |
| | 2 | 146.5 | 146 | 146 | 145.0 |
| | 3 | 233.0 | 232 | 233 | 233.0 |
| | 4 | 314.0 | 313 | 315 | 313.0 |
| | 5 | 362.0 | 368 | 366 | 361.0[b] |
| | 6 | 445.0 | — | 440 | 427.0/445.0[c] |
| | 7 | 535.0 | 536 | 534 | 533.5 |
| $B_{1g}$ | 1 | 112.0 | 111 | — | 111.0 |
| | 2 | 162.0 | 160 | — | 159.0 |
| | 3 | 222.5 | 222 | 223 | 221.0 |
| | 4 | 280.0 | — | — | 278.0 |
| | 5 | 414.0 | 414 | 405 | 412.0 |
| | 6 | 512.0 | 512 | — | 508.0 |
| | 7 | 570.0 | — | — | 566.0 |
| $B_{2g}$ | 1 | 119.0 | — | — | 117.5 |
| | 2 | 146.5 | 146[a] | 146 | 145.0 |
| | 3 | 400.0 | 398 | 399 | 399.0 |
| | 4 | 468.0 | 475 | 470 | 468.0 |
| | 5 | 522.0 | 523 | 522 | 521.0 |
| $B_{3g}$ | 1 | 174.0 | 174 | 172 | 172.0 |
| | 2 | 217.0 | 217 | 215 | 217.0 |
| | 3 | 334.0 | 323 | — | 334.0 |
| | 4 | 400.0 | 400 | 399 | 399.0 |
| | 5 | 551.0 | 551 | — | 547.0 |

[a] Assigned in [28] to the $B_{2g}$ 1 mode. [b] This band is among all bands the one undergoing the largest frequency shift and broadening, indicating that the movement of the $Al^{3+}$/$Cr^{3+}$ ions have a large contribution to the corresponding vibration. [c] The appearance of the additional low-frequency band is, with all probability, a consequence of the $Al^{3+}$ by $Cr^{3+}$ substitution.

before;[28,29] see Table 4). The assignment of all other modes follows those previously suggested.[28,29]

The analysis of the Raman spectra provided new data for the undoped material that allowed for fine tuning of the assignments for that material, and are completely new for the synthesized doped material.

### 3.4 Photoluminescence measurements

**3.4.1 Photoluminescence emission spectrum (PL).** The room temperature PL spectra of $Gd_{0.995}Sm_{0.005}Al_{0.995}Cr_{0.005}O_3$ and $GdAlO_3$ compounds are shown in Fig. 7. The spectra were collected in time-resolved mode (using a pulsed lamp) with excitation at 377 nm and with a 0.05 ms delay after flash. The intense and well-resolved line observed at 726 nm is ascribed to a $Cr^{3+}$ 3d–3d transition from the excited $^2E_g(^2G)$ to the ground $^4A_{2g}(^4F)$ state.[30] This emission, with its remarkable tissue-penetrating capability and minimal tissue damage, makes the synthesized compound a promising candidate for *in vivo* imaging applications and optoelectronic devices.

Additionally, an emission line at 735 nm, commonly observed in systems containing high concentrations of $Cr^{3+}$ ions (*e.g.*, $GaAlO_3$:$Cr^{3+}$, $LaAlO_3$:$Cr^{3+}$ (ref. 31)), is likely due to energy transfer between exchange-coupled $Cr^{3+}$ pairs and individual $Cr^{3+}$ ions. Emission bands observed at 720, 704, 697, and 680 nm are attributed to the $Gd^{3+}$ 4f–4f transitions ($^6P_j \rightarrow {}^8S_{7/2}, j$ = 3/2, 5/2 and 7/2). Bands at 660 nm ($^4G_{5/2} \rightarrow {}^6H_{11/2}$), 647 nm ($^4G_{5/2} \rightarrow {}^6H_{9/2}$), 600 nm ($^4G_{5/2} \rightarrow {}^6H_{7/2}$), and 564 nm ($^4G_{5/2} \rightarrow {}^6H_{5/2}$) are assigned to $Sm^{3+}$ 4f–4f transitions.[32]

**3.4.2 Photoluminescence excitation spectra (PLE).** Fig. 8 presents the PLE spectra of the studied doped material at room temperature, collected with emission at 600 and 697 nm. The spectrum monitored at $\lambda_{em}$ = 697 nm spectra present a narrow UV excitation band corresponding to $Gd^{3+}$ 4f–4f transition, located at 275 nm and assigned to the absorption $^8S_{7/2} \rightarrow {}^6I_{11/2}$, and a broad band located at 326 nm, due to the $^8S_{7/2} \rightarrow {}^6P_j$ transition.[33] Two additional broad bands in the visible region correspond to $Cr^{3+}$ 3d–3d transitions: 564 nm ($^4A_{2g}(^4F) \rightarrow {}^4T_{2g}(^4F)$) and 418 nm ($^4A_{2g}(^4F) \rightarrow {}^4T_{1g}(^4F)$).

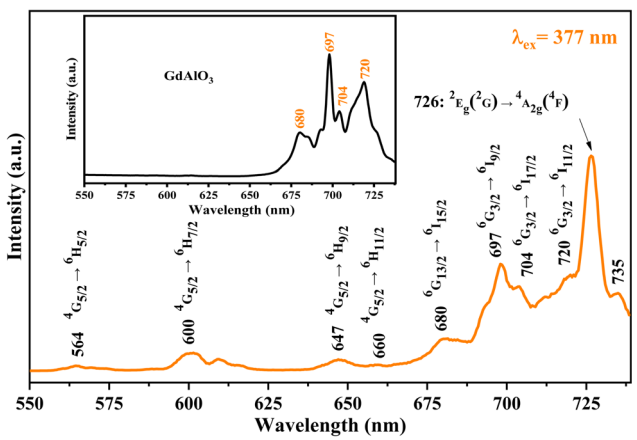


Fig. 7 Comparison between the $GdAlO_3$ and $Gd_{0.995}Sm_{0.005}Al_{0.995}Cr_{0.005}O_3$ PL spectra (collected with excitation at 377 nm).

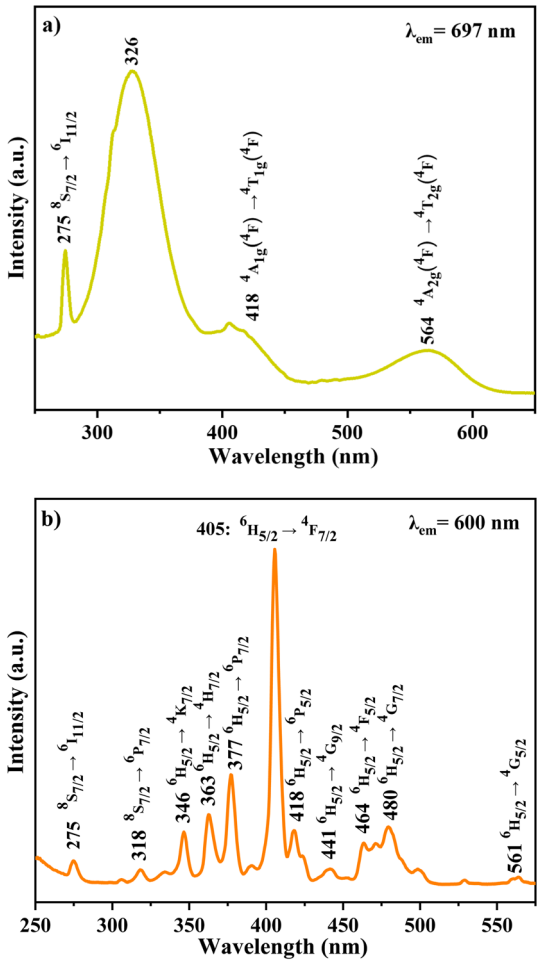


Fig. 8 PLE spectra of the studied doped perovskite monitored at (a) 697 and (b) 600 nm.

In contrast, the PLE spectrum monitored at $\lambda_{em}$ = 600 nm reveals multiple excitation bands above 340 nm, arising from intra-configurational 4f–4f transitions of $Sm^{3+}$.[34] These bands, detailed in Table 5, correspond to transitions from the ground state $^6H_{5/2}$ to various excited states (*e.g.*, $^4K_{7/2}$, $^4H_{7/2}$, $^6P_{7/2}$, $^4F_{7/2}$, $^6P_{5/2}$, $^4G_{9/2}$, $^4F_{5/2}$, $^4G_{7/2}$, $^4G_{5/2}$).[35,36] Weak excitation peaks at 275 nm ($^8S_{7/2} \rightarrow {}^6I_{11/2}$) and 318 nm ($^8S_{7/2} \rightarrow {}^6P_{7/2}$) further confirm the occurrence of energy transfer from $Gd^{3+}$ to $Cr^{3+}$ ions.

Table 5 Excitation transitions of $Gd_{0.995}Sm_{0.005}Al_{0.995}Cr_{0.005}O_3$

| Transition for $Sm^{3+}$ (ion) | Wavelength (nm) |
|---|---|
| $^6H_{5/2} \rightarrow {}^4K_{7/2}$ | 346 |
| $^6H_{5/2} \rightarrow {}^4H_{7/2}$ | 363 |
| $^6H_{5/2} \rightarrow {}^6P_{7/2}$ | 377 |
| $^6H_{5/2} \rightarrow {}^4F_{7/2}$ | 405 |
| $^6H_{5/2} \rightarrow {}^6P_{5/2}$ | 418 |
| $^6H_{5/2} \rightarrow {}^4G_{9/2}$ | 441 |
| $^6H_{5/2} \rightarrow {}^4F_{5/2}$ | 464 |
| $^6H_{5/2} \rightarrow {}^4G_{7/2}$ | 480 |
| $^6H_{5/2} \rightarrow {}^4G_{5/2}$ | 561 |

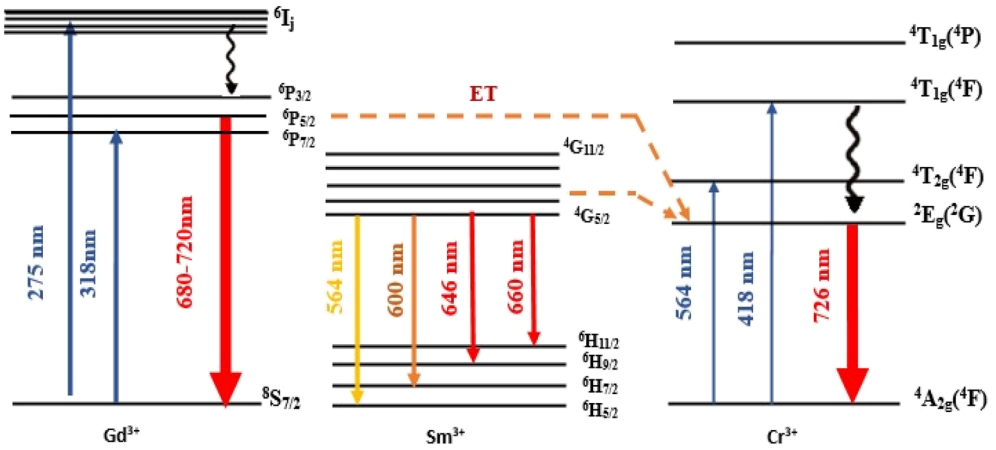


Fig. 9 Energy transfer between $Gd^{3+}$, $Sm^{3+}$ and $Cr^{3+}$ ions.

**3.4.3 Energy transfer mechanism.** The luminescence of $Cr^{3+}$ can be further enhanced by the presence of lanthanides due to the energy transfer (ET) from $Gd^{3+}$ and $Sm^{3+}$ to $Cr^{3+}$. The photoluminescence (PL) spectrum of $GdAlO_3$:$Cr^{3+}$ and $Sm^{3+}$ shows a decrease in the emission intensity of the $Gd^{3+}$ ion at 697 nm and 720 nm ($^6P_J \rightarrow {}^8S_{7/2}$) compared to the emission intensity in the undoped $GdAlO_3$ spectrum (Fig. 7). We also notice that the red line at 726 nm, corresponding to the main luminescence $^2E_g(^2G) \rightarrow {}^4A_{2g}(^4F)$ from $GdAlO_3$:$Cr^{3+}$ and $Sm^{3+}$, is intense. This observation confirms the significant energy transfer from $Gd^{3+}$ and $Sm^{3+}$ ions to the $Cr^{3+}$ dopant ions, which further enhances the luminescence of the $Cr^{3+}$ ions. Energy transfer occurs from the $Gd^{3+}$ emissions at 697 nm and 720 nm ($^6P_J \rightarrow {}^8S_{7/2}$) to the emission of $Cr^{3+}$ ions. Additionally, energy transfer from $Sm^{3+}$ emissions at 564 nm ($^4G_{5/2} \rightarrow {}^6H_{5/2}$; green), 600 nm ($^4G_{5/2} \rightarrow {}^6H_{7/2}$; yellow), 647 nm ($^4G_{5/2} \rightarrow {}^6H_{9/2}$; orange), and 660 nm ($^4G_{5/2} \rightarrow {}^6H_{11/2}$; red) further enhances the $^2E_g(^2G) \rightarrow {}^4A_{2g}(^4F)$ emission as shown in Fig. 9. The higher excited states $^4T_{1g}(^4P)$, $^4T_{1g}(^4F)$, $^4T_{2g}(^4F)$ relax non-radiatively to the lowest excited state $^2E_g(^2G)$ of $Cr^{3+}$, which then undergoes radiative relaxation from the $^2E_g(^2G)$ state to the ground state $^4A_{2g}(^4F)$.

**3.4.4 Potential energy surface.** In transition ion complexes, electronic transitions are essentially electric dipolar in nature. The d–d transitions for transition metal complexes are in principle prohibited by Laporte's rule.[37] Nevertheless, observation of these transitions can be explained by vibronic coupling (coupling between vibrational and electronic wave functions). For example, for an octahedral complex, it can be assumed that some of the vibrations distort the octahedron in such a way that the center of symmetry is destroyed. The states of the configuration $d^n$ then no longer strictly preserve their character $g$ and the transitions, normally prohibited by Laporte's rule, become "slightly permitted".[37] Vibronic origins are mainly associated with odd-parity vibrational modes. Table 6 gives the selection rules for the $Cr^{3+}$ ion occupying an $O_h$ site in the studied doped perovskite. As shown in the table, the $Cr^{3+}$ 3d–3d transitions observed in the PLE (Fig. 10) are governed by the vibronic mechanism that allow non-graded parity modes ($a_{1u}$, $a_{2u}$, $t_{1u}$, $t_{2u}$ and $e_u$).

Table 6 Selection rules for electronic transitions of $Cr^{3+}$ occupying an $O_h$ site symmetry in the studied doped perovskite

| d–d transitions | Electric dipole transition (odd vibrational mode that makes the transition permitted) $\langle \Gamma_i \vert T_{1u} \vert \Gamma_f \rangle \Gamma_u = A_{1g}$ |
|---|---|
| $^4A_{2g}(^4F) \rightarrow {}^4T_{2g}(^4F)$ | $a_{1u}$, $t_{1u}$, $t_{2u}$, $e_u$ |
| $^4A_{2g}(^4F) \rightarrow {}^4T_{1g}(^4F)$ | $a_{2u}$, $t_{1u}$, $t_{2u}$, $e_u$ |

To better understand the absorptions and emissions observed in the PLE and PL spectra of the studied compound, the coupled potential energy surface model was used. To simplify the model, a single normal coordination coordinate $Q$ was considered. Due to the characteristics of the electronic transition, which is an intra-configuration d–d excitation, the potential energy minima of the doublet $^2E_g(^2G)$ and fundamental $^4A_{2g}(^4F)$ states are considered to be at the same configuration ($Q = 0$ Å) and have the same vibrational frequency. As the metal–ligand antibonding molecular orbitals are populated by d–d excitation, the minimum potential energy of the states $^4T_{2g}(^4F)$, $^4T_{1g}(^4F)$ and $^4T_{1g}(^4P)$ is shifted by the quantity $\Delta Q$ relative to the minimum of the $^2E_g(^2G)$ state.

The potentials for the excited states $^2E_g(^2G)$, $^4T_{2g}(^4F)$, $^4T_{1g}(^4F)$ and $^4T_{1g}(^4P)$ are as follows:

$$V(^2E_g(^2G)) = 1/2(kQ^2) + E_{ZPL}(^2E_g(^2G)) \quad (1a)$$

$$V(^4T_{2g}(^4F)) = 1/2(k(Q - \Delta Q_1)^2) + E_{ZPL}(^4T_{2g}(^4F)) \quad (1b)$$

$$V(^4T_{1g}(^4F)) = 1/2(k(Q - \Delta Q_1)^2) + E_{ZPL}(^4T_{1g}(^4F)) \quad (1c)$$

$$V(^4T_{1g}(^4P)) = 1/2(k(Q - \Delta Q_1)^2) + E_{ZPL}(^4T_{1g}(^4P)) \quad (1d)$$

where $E_{ZPL}(^2E_g(^2G))$, $E_{ZPL}(^4T_{2g}(^4F))$, $E_{ZPL}(^4T_{1g}(^4F))$, and $E_{ZPL}(^4T_{1g}(^4P))$ are the energies of the minima for the $^2E_g(^2G)$, $^4T_{2g}(^4F)$, $^4T_{1g}(^4F)$ and $^4T_{1g}(^4P)$ states, respectively, and $k$ is the Raman frequency of $GdAlO_3$ assigned to the ground and excited states. The adiabatic potential state surfaces, obtained from eqn (1) are depicted in Fig. 10.

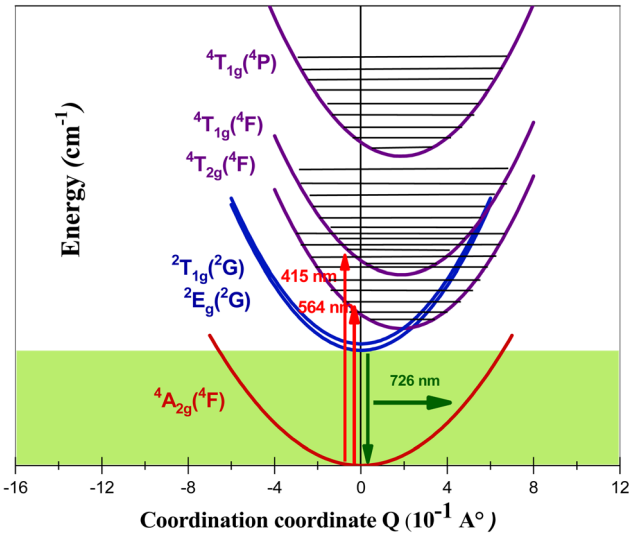


Fig. 10 Adiabatic potential energy curves for $^2E_g(^2G)$, $^4T_{2g}(^4F)$, $^4T_{1g}(^4F)$ and $^4T_{1g}(^4P)$ states.

**3.4.5 Crystal field analysis of $Cr^{3+}$ in $GdAlO_3$ and relevance to PLE and PL spectra.** The electronic structure of $Cr^{3+}$ in $GdAlO_3$ can be ascertained by employing the Crystal Field Theory (CFT). In this work, we expand on previous studies by providing a more detailed analysis of the crystal field effects and their influence on the photoluminescence (PL) behavior of $Cr^{3+}$ in this host material. The $Cr^{3+}$ ion energy levels are assessed using a complete Hamiltonian, and the crystal field strength ($D_q$), as well as the Racah parameters ($B$ and $C$), are found by analyzing the optical PLE and PL spectra.

The $Cr^{3+}$ ion energy levels are assessed using the complete Hamiltonian:[38–50]

$$H = H_0 + H_{ee}(B, C) + H_{Trees}(\alpha_{Trees}) + H_{CF}(D_q) + H_{SO}(\zeta) \quad (2)$$

where $H_0$ is the configuration Hamiltonian, $H_{ee}$ is the electron–electron repulsion Hamiltonian,[51–53] $H_{SO}$ is the spin–orbit coupling Hamiltonian, the $H_{Trees}$ Hamiltonian included the Trees correction,[54,55] and $H_{CF}$ is the crystal field Hamiltonian for octahedral symmetry ($O_h$):[56–58]

$$H_{CF} = 21D_q\left[C_0^{(4)} + \sqrt{\frac{5}{14}}\left(C_0^{(4)} + C_{-4}^{(4)}\right)\right] \quad (3)$$

In eqn (2) and (3) the parameter $D_q$ represents the ligand field splitting, while numerical techniques are used to specifically calculate the matrix elements for the $C_q(k)$ operators, as described in ref. 59. The $\alpha_{Trees}$ and $\zeta$ parameters are calculated using the following equations:[54–56]

$$\alpha_{Trees} = N^4\alpha_0$$

and

$$\zeta = N^2\zeta_0 \quad (4)$$

with:

$$N^2 = \frac{1}{2}\left(\sqrt{\frac{B}{B_0}} + \sqrt{\frac{C}{C_0}}\right) \quad (5)$$

where, $N$ is the reduction factor.[60]

Table 7 Optical parameter values for the theoretical study of $GdAlO_3:Cr^{3+}$

| Parameter | Value [this study] | Parameter | Value[43,51] |
|---|---|---|---|
| $D_q$ ($cm^{-1}$) | 1773 | $B_0$ ($cm^{-1}$) | 918 |
| $B$ ($cm^{-1}$) | 617 | $C_0$ ($cm^{-1}$) | 4133 |
| $C$ ($cm^{-1}$) | 3045 | $\alpha_0$ | 30 |
| $\alpha$ ($cm^{-1}$) | 21.12 | $\zeta_0$ | 275 |
| $\zeta$ ($cm^{-1}$) | 230.75 | | |
| $D_q/B$ | 2.87 | | |
| $C/B$ | 4.94 | | |

Table 8 Experimental and calculated energies ($cm^{-1}$) of $GdAlO_3:Cr^{3+}$

| $O_h$ | $E_{obs}$ | $E^*_{cal}$ [this work] | $E^{a*}_{cal}$ [this work] |
|---|---|---|---|
| $^4A_{2g}(^4F)$ | 0 | 0 | 0 |
| $^2E_g(^2G)$ | — | 13 767 | 13 896 (4) |
| $^2T_{1g}(^2G)$ | | 14 282 | 14 404 (4) |
| | | | 14 461 (2) |
| $^4T_{2g}(^4F)$ | 17 730 | 17 730 | 17 637 (2) |
| | | | 17 692 (4) |
| | | | 17 802 (2) |
| | | | 17 806 (4) |
| $^2T_{2g}(^2G)$ | — | 20 897 | 20 966 (4) |
| | | | 21 072 (2) |
| $^4T_{1g}(^4F)$ | 23 923 | 24 097 | 23 988 (4) |
| | | | 23 997 (2) |
| | | | 24 002 (2) |
| | | | 24 006 (4) |
| $^2A_{1g}(^2G)$ | — | 29 333 | 29 514 (2) |
| $^2T_{1g}(^2P)$ | — | 31 342 | 31 541 (2) |
| | | | 31 587 (4) |
| $^2T_{1g}(^2H)$ | — | 31 653 | 31 744 (2) |
| | | | 31 918 (4) |
| $^2E_g(^2H)$ | — | 33 266 | 33 397 (4) |
| $^2T_{1g}(^2H)$ | — | 36 101 | 36 161 (2) |
| | | | 36 196 (4) |
| $^4T_{1g}(^4P)$ | — | 38 348 | 38 208 (2) |
| | | | 38 223 (4) |
| | | | 38 326 (4) |
| | | | 38 361 (2) |
| $^2T_{2g}(^2H)$ | — | 40 349 | 40 252 (2) |
| | | | 40 355 (4) |
| $^2A_{2g}(^2F)$ | — | 41 673 | 41 683 (2) |
| $^2T_{2g}(^2_aD)$ | — | 49 008 | 49 258 (2) |
| | | | 49 369 (4) |
| $^2T_{2g}(^2F)$ | — | 50 418 | 50 335 (4) |
| | | | 50 455 (2) |
| $^2E_g(^2_aD)$ | — | 50 334 | 50 564 (4) |
| $^2T_{1g}(^2F)$ | — | 54 944 | 54 841 (2) |
| | | | 54 966 (4) |
| $^2T_{2g}(^2_bD)$ | — | 68 763 | 68 605 (4) |
| | | | 68 804 (2) |
| $^2E_g(^2_bD)$ | — | 72 704 | 72 761 (4) |

We derived a stable crystal-field and Racah parameters for $Cr^{3+}$ ions, which allow to calculate the electronic energy levels of $Cr^{3+}(3d^3)$ ions in the $O_h$ symmetry site of a $Cr^{3+}$ doped $GdAlO_3$ perovskite ($GdAlO_3$:$Cr^{3+}$). The free ion $Cr^{3+}$ parameters $B_0$, $C_0$, $\alpha_0$ and $\zeta_0$ are listed in Table 7.[41–43] The crystal-field strength parameter $D_q$ was computed using the energy of the quartet excited state $^4T_{2g}(^4F)$, and the Racah parameters $B$ and $C$ were calculated based on the observed excited states of the $^4T_{1g}(^4F)$ quartet and the $^2E_g(^2G)$ doublet, decreasing in relation to their values for the free ion due to the covalency effect. The values of $\alpha$ and $\zeta$ were obtained using eqn (3)–(5). The calculations were done using a custom code that was developed in our laboratory, by S. Kammoun, using the Maple 2024 software. The calculated energies (Table 8) are in excellent agreement with the experimental findings of Yeung *et al.*,[61] thus validating our computational method.

Electrons are usually transferred from one atom to another during ionic bonding, producing positively and negatively charged ions. Eqn (6) allows to evaluate the type of bonding for $Cr^{3+}$ in $GdAlO_3$:$Cr^{3+}$.[62] In this equation, $h$ is a measure of the degree of electron delocalization between the cation to the ligands. For the considered system, the constant $k$ is equal to 0.21.[63,64]

$$h = \left[\frac{B_0 - B}{B_0 k}\right] \quad (6)$$

The calculated large value for $h$ (1.44) indicates a high degree of d-electron delocalization, revealing the high ionic character of the bonds established between $Cr^{3+}$ ions and their ligands.

The basic optical characteristics of $3d^n$ transition-metal ions doped into crystalline hosts can be explained by the crystal-field model. The Tanabe–Sugano energy-level diagram presented in Fig. 11 shows how the ratio $D_q/B$ affects the electronic energy levels of $3d^n$ trivalent ionic species in the octahedral site of the $GdAlO_3$ host. The vertical line in Fig. 11 for $D_q/B = 2.87$ corresponds to $Cr^{3+}$ doped into the $GdAlO_3$ perovskite in an octahedral site symmetry.

The theoretical study for determining the electronic structure of $Cr^{3+}$ ion in $GdAlO_3$:Cr,Sm using crystal field theory confirms that this ion replaces $Al^{3+}$ at an octahedral site. Indeed, there is a satisfactory agreement between the experimental and theoretical levels, considering that $Cr^{3+}$ replaces $Al^{3+}$ at an octahedral site. The importance of the theoretical study using crystal field theory lies in the fact that it confirms the oxidation state and the site occupied by the $Cr^{3+}$ ion. Also, it is only through this theoretical study that the d–d transitions can be accurately assigned, as these transitions vary for the same ion depending on the matrix (intermediate crystal field).

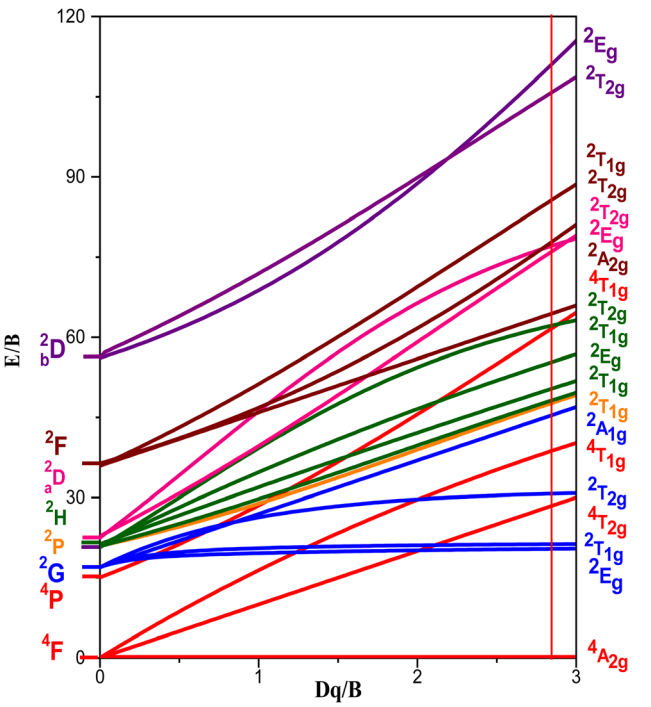


Fig. 11 Tanabe–Sugano energy-levels diagram highlighting the case of $Cr^{3+}(3d^3)$ ion doped into the octahedral symmetry site of $GdAlO_3$, as expressed by the vertical line for $D_q/B = 2.87$.

## 4. Conclusion

In conclusion, the orthorhombic $Gd_{0.995}Sm_{0.005}Al_{0.995}Cr_{0.005}O_3$ sample, synthesized through the solid-state reaction method, underwent comprehensive investigation of its structure, morphology, and photoluminescence properties. The material crystallized in the orthorhombic *Pbnm* space group, with $Cr^{3+}$ ions substituting for $Al^{3+}$ ions in octahedral site symmetry within the $GdAlO_3$:$Sm^{3+}$, $Cr^{3+}$ matrix. Examination *via* Scanning Electron Microscopy (SEM) and Energy Dispersive X-ray analysis confirmed the morphology and homogeneity of the sample's chemical composition. Photoluminescence excitation (PLE) and photoluminescence (PL) spectra revealed the electronic structure of $Cr^{3+}$ ions in the $O_h$ symmetry site, with theoretical studies allowing for precise attribution of their 3d–3d transitions. Additionally, intra-configurational 4f–4f transitions of $Sm^{3+}$ resulted in various excitation bands observed in the PLE spectrum at higher wavelengths. Moreover, the photoluminescence studies give additional support to the occurrence of energy transfer among $Gd^{3+}$, $Sm^{3+}$, and $Cr^{3+}$ ions. Based on these findings, the synthesized nanophosphor samples demonstrate strong potential for applications in solid-state lighting.

## Data availability

Data are available upon request to the authors.

## Conflicts of interest

The authors declare that they have no known competing financial interests or personal relationships that could have appeared to influence the work reported in this paper.

## Acknowledgements

The CQC-IMS is supported by FCT through projects UI0313B/QUI/2020, UI0313P/QUI/2020 and LA/P/0056/2020 (national funds). This work was also supported by FCT – Fundação para a Ciência e Tecnologia, I. P. through the projects UIDB/04564/2020 and UIDP/04564/2020, with DOI identifiers 10.54499/UIDB/04564/2020 and 10.54499/UIDP/04564/2020, respectively. Access to TAIL-UC facility funded under QREN-Mais Centro Project No. ICT_2009_02_012_1890 is gratefully acknowledged.

## References

1 R. E. Rojas-Hernandez, F. Rubio-Marcos, M. A. Rodriguez and J. F. Fernandez, Long lasting phosphors: $SrAl_2O_4$:Eu, Dy as the most studied material, *Renewable Sustainable Energy Rev.*, 2018, **81**, 2759–2770.

2 D. Singh, V. Tanwar, S. Bhagwan and I. Singh, Recent advancements in luminescent materials and their potential applications, *Adv. Magn. Opt. Mater.*, 2016, 317–352.

3 P. Kumar, D. Singh, I. Gupta, S. Singh, V. Kumar, H. Kumar and S. K. Chhikara, Cool green light emitting $GdAlO_3$:$Tb^{3+}$ perovskite nanomaterials: crystal structure and spectroscopic characteristics for advance display appliances, *Inorg. Chem. Commun.*, 2022, **154**, 110064.

4 I. Gupta, S. Singh, S. Bhagwan and D. Singh, Rare earth (RE) doped phosphors and their emerging applications: a review, *Ceram. Int.*, 2021, **47**, 19282–19303.

5 P. Kumar, D. Singh, I. Gupta, S. Singh, V. Kumar, H. Kumar and S. K. Chhikara, Perovskite $GdAlO_3$:$Dy^{3+}$ nanophosphors: a gel-combustion synthesis, phase evaluation and down conversion luminescent characteristics for lighting applications, *J. Lumin.*, 2022, **252**, 119409.

6 K. M. Girish, S. C. Prashantha and H. Nagabhushana, Facile combustion based engineering of novel white light emitting $Zn_2TiO_4$:$Dy^{3+}$ nanophosphors for display and forensic applications, *J. Sci.:Adv. Mater. Devices*, 2017, **2**, 360–370.

7 P. Kumar, S. Singh, I. Gupta, V. Kumar and D. Singh, Luminous $LaAlO_3$:$Dy^{3+}$ perovskite nanomaterials: synthesis, structural and luminescent characteristics for WLEDs, *Luminescence*, 2022, **37**, 1932–1941.

8 E. Pavitra, G. S. R. Raju, G. L. Varaprasad, N. R. Chodankar, M. V. B. Rao, N. M. Rao, J. Y. Park, Y.-K. Han and Y. S. Huh, Desired warm white light emission from a highly photostable and single-component $Gd_2TiO_5$:$Dy^{3+}$/$Eu^{3+}$ nanophosphors for indoor illuminations, *J. Alloys Compd.*, 2021, **875**, 160019.

9 P. Kumar, S. Singh, I. Gupta, V. Kumar and D. Singh, Preparation and luminescence behaviour of perovskite $LaAlO_3$:$Tb^{3+}$ nanophosphors for innovative displays, *Optik*, 2022, **267**, 169709.

10 P. Kumar, S. Singh, I. Gupta, A. Dalal, V. Kumar and D. Singh, Preparation, structural and photometric properties of single-phased $Gd_3Al_5O_{12}$:$Tb^{3+}$ green-emitting phosphors for solid state lighting purpose, *Mater. Sci. Eng., B*, 2023, **288**, 116189.

11 V. Tanwar, S. Singh, I. Gupta, P. Kumar, H. Kumar, B. Mari and D. Singh, Preparation and luminescence characterization of Eu(III)-activated Forsterite for optoelectronic applications, *J. Mol. Struct.*, 2022, **1250**, 131802.

12 I. Gupta, P. Kumar, S. Singh, S. Bhagwan, S. K. Chhikara and D. Singh, Synthesis, structural and optical investigations of $YAlO_3$:$Er^{3+}$ perovskites for near UV pumped photonic appliances, *Inorg. Chim. Acta*, 2022, **543**, 121183.

13 D. Singh, S. Sheoran and J. Singh, Optical characterization of $Eu^{3+}$ doped $MLSiO_4$ (M = Ca, Sr, Ba and L = Mg) phosphor materials for display devices, *J. Mater. Sci.: Mater. Electron.*, 2018, **29**, 294–302.

14 I. Gupta, D. Singh, S. Singh, P. Kumar, S. Bhagwan and V. Kumar, Study of structural and spectroscopic characteristics of novel color tunable yellowish-white $Dy^{3+}$ doped $Gd_4Al_2O_9$ nanophosphors for NUV-based WLEDs, *J. Mol. Struct.*, 2022, **1272**, 134199.

15 Y. Wu, X. Yin, Q. Zhang, W. Wang and X. Mu, The recycling of rare earths from waste tricolor phosphors in fluorescent lamps: a review of processes and technologies, *Resour., Conserv. Recycl.*, 2014, **88**, 21–31.

16 I. Gupta, D. Singh, S. Singh, P. Kumar, S. Bhagwan and V. Kumar, Phase recognition and spectroscopic characteristics of single-phase $Tb^{3+}$ doped $Gd_4Al_2O_9$ nanophosphors for NUV energized advanced photonic appliances, *J. Lumin.*, 2022, **252**, 119327.

17 R. K. Sajwan, S. Tiwari, T. Harshit and A. K. Singh, Recent progress in multicolor tuning of rare earth-doped gadolinium aluminate phosphors $GdAlO_3$, *Opt. Quantum Electron.*, 2017, **49**, 344.

18 J. I. Eldridge, Single fiber temperature probe configuration using anti-Stokes luminescence from Cr:$GdAlO_3$, *Meas. Sci. Technol.*, 2018, **29**, 065206.

19 S. Adachi, Review – Photoluminescence properties of $Cr^{3+}$-activated oxide phosphors, *ECS J. Solid State Sci. Technol.*, 2021, **10**, 026001.

20 P. Dorenbos, E. Bougrine, J. D. Haas, C. Eijk and M. Korzhik, Scintillation properties of $GdAlO_3$:Ce crystals, *Radiat. Eff. Defects Solids*, 1995, **135**, 321–323.

21 M. Y. Gneber, I. Elhamdi, J. Messoudi, R. Dhahri, F. Sahnoune, M. Jemmali, M. Hussein, E. Dhahri and B. F. O. Costa, Investigation of variable range hopping and dielectric relaxation in $GdCrO_3$ orthochromite perovskites, *RSC Adv.*, 2024, **14**, 36161–36172.

22 K. Momma and F. Izumi, VESTA 3 for three-dimensional visualization of crystal, volumetric and morphology data, *J. Appl. Crystallogr.*, 2011, **44**, 1272–1276.

23 I. Elhamdi, H. Souissi, O. Taktak, S. Kammoun, E. Dhahri, J. Pina, B. F. O. Costa and E. López-Lago, Optical characterization and defect-induced behavior in $ZnAl_{1.999}Ho_{0.001}O_4$ spinel: unraveling novel insights into structure, morphology, and spectroscopic features, *Heliyon*, 2024, **10**, E29241.

24 I. Elhamdi, F. Mselmi, H. Souissi, S. Kammoun, E. Dhahri, P. Sanguino and B. F. O. Costa, Summerfield scaling model and electrical conductivity study for understanding

transport mechanisms of a $Cr^{3+}$ substituted $ZnAl_2O_4$ ceramic, *RSC Adv.*, 2023, **13**, 3377–3393.

25 F. Mselmi, I. Elhamdi, M. Bejar and E. Dhahri, Cross-relaxation induced efficient 1.55 μm emission in $La_{1.95}Er_{0.05}Ti_2O_7$ towards an application as an amplifier for silica-fibers, *Opt. Mater.*, 2023, **137**, 113555.

26 C. S. McCamy, Correlated color temperature as an explicit function of chromaticity coordinates, *Color. Res. Appl.*, 1992, **17**, 142–144.

27 S. Sun and Q. Xu, Fabricating a novel intragranular microstructure for $Al_2O_3/GdAlO_3$ ceramic composites, *Materials*, 2018, **11**, 1879.

28 A. Chopelas, Single-crystal Raman spectra of $YAlO_3$ and $GdAlO_3$: comparison to several orthorhombic $ABO_3$ perovskites, *Phys. Chem. Miner.*, 2011, **38**, 709–726.

29 G. Gouadec, P. Colomban, N. Piquet, M. F. Trichet and L. Mazerolles, Raman/$Cr^{3+}$ fluorescence mapping of a melt-grown $Al_2O_3/GdAlO_3$ eutectic, *J. Eur. Ceram. Soc.*, 2005, **25**, 1447–1453.

30 G. Wei, P. Li, R. Li, Y. Wang, S. He, J. Li, Y. Shi, H. Suo, Y. Yang and Z. Wang, How to Achieve Excellent Luminescence Properties of Cr Ion-Doped Near-Infrared Phosphors, *Adv. Opt. Mater.*, 2023, **11**, 2301794.

31 H. Luo and P. Dorenbos, The dual role of $Cr^{3+}$ in trapping holes and electrons in lanthanide co-doped $GdAlO_3$ and $LaAlO_3$, *J. Mater. Chem. C*, 2018, **6**, 4977–4984.

32 N. Wantana, S. Kaewjaeng, S. Kothan, H. J. Kim and J. Kaewkhao, Energy transfer from $Gd^{3+}$ to $Sm^{3+}$ and luminescence characteristics of $CaO–Gd_2O_3–SiO_2–B_2O_3$ scintillating glasses, *J. Lumin.*, 2017, **181**, 382–386.

33 J. Li, J. G. Li, J. Li, S. Liu, X. Li, X. Sun and Y. Sakka, Development of $Eu^{3+}$ activated monoclinic, perovskite, and garnet compounds in the $Gd_2O_3–Al_2O_3$ phase diagram as efficient red-emitting phosphors, *J. Solid State Chem.*, 2013, **206**, 104–112.

34 R. Cao, M. Wu, B. Lan, T. Huang, J. Nie, F. Cheng, X. Luo and J. Wang, Study on the properties of $Sm^{3+}$-Doped $CaTbAl_3O_7$ phosphors, *J. Lumin.*, 2025, **277**, 120898.

35 P. Kumar, D. Singh, I. Gupta, S. Singh and V. Kumar, Structural and luminescent characteristics of orthorhombic $GdAlO_3$:$Sm^{3+}$ nanocrystalline materials for solid state lighting, *Chem. Phys. Lett.*, 2023, **812**, 140277.

36 P. Kumar, D. Singhlogo and I. Gupta, Gadolinium-based $Sm^{3+}$ activated $GdSr_2AlO_5$ nanophosphor: synthesis, crystallographic and opto-electronic analysis for warm LEDs, *RSC Adv.*, 2023, **13**, 7703–7718.

37 O. Kahn, *Structure electrónique des eléments de transitions*, Presses Universitaires de France, Paris, 1997.

38 O. Taktak, H. Souissi and S. Kammoun, Optical absorption properties of $ZnF_2$-RO-$TeO_2$ (R = Pb, Cd and Zn) glasses doped with chromium (III): Neuhauser model and crystal field study, *Opt. Mater.*, 2021, **113**, 110682.

39 H. Souissi, O. Taktak and S. Kammoun, Crystal field study of chromium (III) ions doped antimony phosphate glass: Fano's antiresonance and Neuhauser models, *Indian J. Phys.*, 2018, **92**, 1153–1160.

40 O. Maalej, O. Taktak, B. Boulard and S. Kammoun, Study with analytical equations of absorption spectra containing interference dips in fluoride glasses doped with $Cr^{3+}$, *J. Phys. Chem. B*, 2016, **120**, 7538–7545.

41 S. Kammoun and J. El Ghoul, Structural and optical investigation of Co-doped ZnO nanoparticles for nano optoelectronic devices, *J. Mater. Sci.: Mater. Electron.*, 2021, **32**, 7215–7225.

42 A. Neffati, H. Souissi and S. Kammoun, Electronic structure of Co-doped ZnO nanorods, *J. Appl. Phys.*, 2012, **112**, 083112.

43 F. Mselmi, A. Neffatiand and S. Kammoun, Theoretical investigation of the cathodoluminescence spectra of Co-doped ZnO nanowires, *J. Lumin.*, 2018, **198**, 124–131.

44 F. Mselmi, O. Taktak, H. Souissi and S. Kammoun, Correlation between experimental spectroscopic study and crystal-field calculations of $Co^{2+}$ ions in α-$ZnAl_2S_4$ spinel, *J. Lumin.*, 2019, **206**, 319–325.

45 I. Elhamdi, H. Souissi, S. Kammoun, E. Dhahri, J. Pina, B. F. O. Costa and E. López-Lago, Comprehensive characterization and optoelectronic significance of $Ho^{3+}$ and $Cr^{3+}$ Co-doped $ZnAl_2O_4$ spinels, *Dalton Trans.*, 2024, **53**, 7721–7733.

46 I. Elhamdi, H. Souissi, S. Kammoun, E. Dhahri, A. L. B. Brito, R. Fausto and B. F. O. Costa, Experimental determination and modeling of structural, vibrational and optical properties of the $ZnAl_{2-x}Cr_xO_4$ ($x$ = 0 and 0.05) spinels, *J. Lumin.*, 2023, **263**, 119968.

47 I. Elhamdi, F. Mselmi, S. Kammoun, E. Dhahri, A. J. Carvalho, P. Tavares and B. F. O. Costa, A far-red-emitting $ZnAl_{1.95}Cr_{0.05}O_4$ phosphor for plant growth LED applications, *Dalton Trans.*, 2023, **52**, 9301–9314.

48 O. Taktak, H. Souissi, I. Elhamdi, A. Oueslati, S. Kammoun, M. Gargouri and E. Dhahri, Optical investigations and theoretical simulation of organic-inorganic hybrid: TPA-$CoCl_4$, *Opt. Mater.*, 2024, **150**, 115251.

49 H. Souissi, S. Kammoun, E. Dhahri and E. López-Lago, Optical and theoretical study of $NaCr(P_2O_7)$: a look through the Neuhauser model and Racah theory, *Dalton Trans.*, 2024, **53**, 14422–14432.

50 H. Souissi, S. Kammoun, E. Dhahri, E. López-Lago and B. F. O. Costa, Exploring the structural and optical properties of lithium-chromium phosphate $Li_3Cr_2(PO_3)_4$, *Heliyon*, 2024, **10**, e36188.

51 S. Sugano, Y. Tanabe and H. Kamimura, *Multiplets of Transition-Metal Ions in Crystals*, Academic Press, New York, USA, 1970.

52 J. S. Griffith, *The Theory of Transition-Metal Ions*, Cambridge University Press, Cambridge, UK, 1961.

53 R. C. Powell, *Physics of Solid-State Laser Materials*, Springer-Verlag, New York, USA, 1st edn, 1998, pp. 215–233.

54 Z.-Y. Yang, C. Rudowicz and Y.-Y. Yeung, Microscopic spin-Hamiltonian parameters and crystal field energy levels for the low $C_3$ symmetry $Ni^{2+}$ centre in $LiNbO_3$ crystals, *Phys. B*, 2004, **348**, 151–159.

55 C. Rudowicz, Z.-Y. Yang, Y.-Y. Yeung and J. Qin, Crystal field and microscopic spin Hamiltonians approach including spin–spin and spin–other-orbit interactions for $d^2$ and $d^8$

ions at low symmetry $C_3$ symmetry sites: $V^{3+}$ in $Al_2O_3$, *J. Phys. Chem. Solids*, 2003, **64**, 1419–1428.

56 D. J. Newman, B. Ng, *Crystal Field Handbook*, Cambridge University Press, Cambridge, UK, 1st edn, 2000, pp. 28–36.

57 B. G. Wybourne, *Spectroscopic Properties of Rare Earth*, Wiley, New York, USA, 1965, 1st edn, pp. 48–234.

58 I. Elhamdi, H. Souissi, O. Taktak, J. Elghoul, S. Kammoun, E. Dhahri and B. F. Costa, Experimental and modeling study of ZnO: Ni nanoparticles for near-infrared light emitting diodes, *RSC Adv.*, 2022, **12**, 13074–13086.

59 J. P. Elliott, B. R. Judd and W. A. Runciman, Energy levels in rare-earth ions, *Proc. R. Soc. London, Ser. A*, 1957, **240**, 509–523.

60 M. G. Zhao, J. A. Xu, G. R. Bai and H. S. Xie, d-orbital theory and high-pressure effects upon the EPR spectrum of ruby, *Phys. Rev. B:Condens. Matter Mater. Phys.*, 1983, **27**, 1516–1522.

61 Y. Y. Yeung and C. Rudowicz, Ligand field analysis of the 3dN ions at orthorhombic or higher symmetry sites, *Comput. Chem.*, 1992, **16**, 207–216.

62 W. Seeber, D. Ehrt and H. Eberdorff-Heidepriem, Spectroscopic and laser properties of $Ce^{3+}/Cr^{3+}/Nd^{3+}$ co-doped fluoride phosphate and phosphate glasses, *J. Non-Cryst. Solids*, 1994, **171**, 94–104.

63 C. K. Jorgensen, *Absorption Spectra and Chemical Bonding in Complexes*, Pergamon Press, London, UK, 1963, p. 113.

64 V. Mahalingam and J. Thirumalai, Effect of co-doping of alkali metal ions on $Ca_{0.5}RE_{1-x}(MoO_4)_2{:}xEu^{3+}$ (RE = Y, La) phosphors with enhanced luminescence properties, *RSC Adv.*, 2016, **6**, 80390–80397.